PNAS RESEARCH ARTICLE | ENGINEERING

Structural state governs the mechanism of shear-band propagation in metallic glasses

Jinhua Yu[a], Zhen Zhang[b], Zhendong Sha[c], Jun Ding[a,1], A. Lindsay Greer[d,e], and Evan Ma[a,1]

Affiliations are included on p. 8.

Edited by Pablo Debenedetti, Princeton University, Princeton, NJ; received December 26, 2024; accepted June 2, 2025

Shear bands (SBs) play a critical role in determining the mechanical behavior of metallic glasses (MGs). However, the rapid dynamics and highly localized nature of SB propagation present significant challenges for direct observation of their atomistic mechanisms using experimental techniques. In this study, we employ hybrid molecular dynamics/Monte Carlo simulations to investigate the atomic-scale mechanisms of SB propagation in $Mg_{65}Cu_{25}Y_{10}$ MGs, prepared using cooling rates as slow as 10^4 K s^{-1}—comparable to experimental casting conditions and significantly slower than the 10^{10} K s^{-1} rates previously employed in atomistic simulations. Our results reveal a qualitative shift in SB propagation mechanisms as the structural state evolves with decreasing cooling rates. In hyperquenched MGs, SB propagation occurs intermittently, characterized by a "stop-and-go" motion driven by sequential activation and coalescence of multiple shear transformation zones (STZs) separated by vortex-like fields. In contrast, slowly cooled MGs exhibit continuous and rapid SB propagation, mediated by localized shear softening and the formation of large vortex fields, indicative of a more collective structural response. This transition arises from significant differences in the number density and spatial distribution of activated STZs across different structural states. These findings provide insights into the microscopic dynamics of SB initiation and propagation in MGs, highlighting how the structural state can be strategically tuned to control SB behavior. This opens up different opportunities for optimizing the mechanical performance of MGs for targeted engineering applications.

metallic glass | shear band | atomistic simulation | shear transformation zone

Significance

Shear bands (SBs) are critical to understanding how metallic glasses (MGs) deform, influencing their strength, ductility, and broader usability in advanced engineering applications. Despite their importance, the microscopic mechanisms of SB propagation remain elusive due to experimental challenges and limitations in previous simulations, which focused on unrealistically fast cooling rates. This study bridges that gap by revealing a qualitative shift in SB propagation mechanisms across a range of cooling rates, including those replicating experimental casting conditions. Our findings demonstrate how the structural state, determined by cooling rate, governs SB behavior, offering a pathway to tailor the mechanical properties of MGs. This work provides both fundamental insights and practical strategies for designing high-performance MGs for next-generation technologies.

Shear bands (SBs) are a ubiquitous feature of localized plastic deformation in metallic glasses (MGs) at room temperature (1–5), playing a critical role in determining their plasticity including yield behavior. The initiation and propagation of SBs in MGs are closely associated with the activation and percolation of shear transformation zones (STZs), which act as the primary mediators of plastic flow when the applied stress surpasses the material's elastic limit (6–9). Several theoretical frameworks, including dislocation theory (10, 11), Eshelby inclusions (12, 13), and shear-crack models (14–16), have been proposed to explain the characteristics of SB propagation. Among these, the STZ vortex mechanism has gained widespread acceptance, suggesting that SBs form due to an Eshelby-like rotational field generated around an activated STZ, which triggers the sequential activation of additional STZs in a self-catalytic process (17–20). Experimental observations of density variations and vortex-like motions support this model (18, 21, 22); however, those characterizations are far removed from the microscopic mechanisms underlying shear banding. These findings suggest that complex mechanisms may govern SB propagation, and further investigation is needed to fully understand and clarify the dynamic evolution of a SB.

The challenges in studying SB propagation arise from their rapid dynamics and highly localized nature, which complicate direct observation of their mechanisms through experimental methods (23–25). As a result, computational approaches, particularly molecular-dynamics (MD) simulations, have become essential tools for exploring the atomistic processes underlying SB formation and propagation in MGs (26–28). However, these methods have limitations, notably the discrepancy between the timescales of simulations and real-world experiments. MD simulations typically employ cooling rates exceeding 10^{10} K s^{-1}, far higher than the cooling rates used in experimental settings, which are generally below 10^4 K s^{-1} (29–32). This difference results in simulated MGs that are mechanically "softer" and exhibit greater plasticity compared to those produced under conventional experimental conditions. Such a focus on highly plastic MG models in prior simulations have left a blank in understanding the behavior of SBs in experimentally relevant MGs.

Author contributions: J.D. and E.M. designed research; J.Y. performed research; J.Y., Z.Z., Z.S., J.D., A.L.G., and E.M. analyzed data; and J.Y., Z.Z., Z.S., J.D., A.L.G., and E.M. wrote the paper.

The authors declare no competing interest.

This article is a PNAS Direct Submission.

[1]To whom correspondence may be addressed. Email: dingsn@xjtu.edu.cn or maen@xjtu.edu.cn.

This article contains supporting information online at https://www.pnas.org/lookup/suppl/doi:10.1073/pnas.2427082122/-/DCSupplemental.

Published July 1, 2025.

In this work, to fill this gap and achieve a comprehensive understanding of shear-banding that closely aligns with experimental MGs, we use a combined approach of MD and Monte Carlo (MC) simulations to create $Mg_{65}Cu_{25}Y_{10}$ MG models with a wide range of mechanical properties (33–36). This approach allows for a detailed examination of the microscopic mechanisms of shear banding across different regimes. Our results show that SB propagation in MGs is governed by fundamentally different mechanisms depending on the structural state of the samples. In slowly cooled MGs, the SB propagation mode is distinctly different from those observed in hyperquenched MGs, and the mechanisms are characterized by different STZ activation energies, structural rearrangements, and stress distributions. These findings are crucial for advancing the fundamental understanding of SB behavior in MGs and for guiding the design and engineering of MGs with optimized mechanical properties for specific applications.

Results and Discussion

MGs Prepared Using Various Effective Cooling Rates. $Mg_{65}Cu_{25}Y_{10}$ serves as a representative example of a brittle MG that has been extensively studied experimentally. In contrast, $Mg_{65}Cu_{25}Y_{10}$ MGs simulated using classical MD exhibit high plasticity with STZ events all over the sample. This inconsistency with experimental observations has been attributed to the extremely high cooling rates (approximately 10^{10} K s^{-1}) used to make the MG model-sample, due to the limited timescale accessible in conventional atomistic simulations. Recent advances in computational techniques, such as the hybrid MD/MC approach, have been developed to bridge the gap between experimental and simulated cooling rates for MGs (36). In this study, we generated a series of $Mg_{65}Cu_{25}Y_{10}$ MG model-samples using both MD and hybrid MD/MC simulations to achieve a wide range of cooling rates, spanning over nine orders of magnitude (as detailed in the *Methods* section).

Fig. 1*A* shows the per-atom atomic potential energy as a function of temperature for various $Mg_{65}Cu_{25}Y_{10}$ MG model samples. The lowest cooling rate for the MD simulations reached ~10^9 K s^{-1}, whereas the cooling curves from the hybrid MD/MC simulations indicate significantly slower quenching rates, as inferred from the glass transition temperature (T_g) and the potential energy of the glassy states. Fig. 1*B* demonstrates that the effective cooling rates of $Mg_{65}Cu_{25}Y_{10}$ MG model-samples prepared using hybrid MD/MC simulations can be obtained by extrapolation from the dependence of potential energy on the cooling rate (36). Notably, the hybrid MD/MC approach significantly reduces the potential energy, achieving effective cooling rates as low as 4×10^4 K s^{-1}, close to the experimental quenching rates used for producing Mg-based bulk MGs.

Through this approach, we prepared a range of $Mg_{65}Cu_{25}Y_{10}$ MG model-samples with effective cooling rates spanning over nine orders of magnitude, from 4×10^4 to 10^{13} K s^{-1}. A detailed

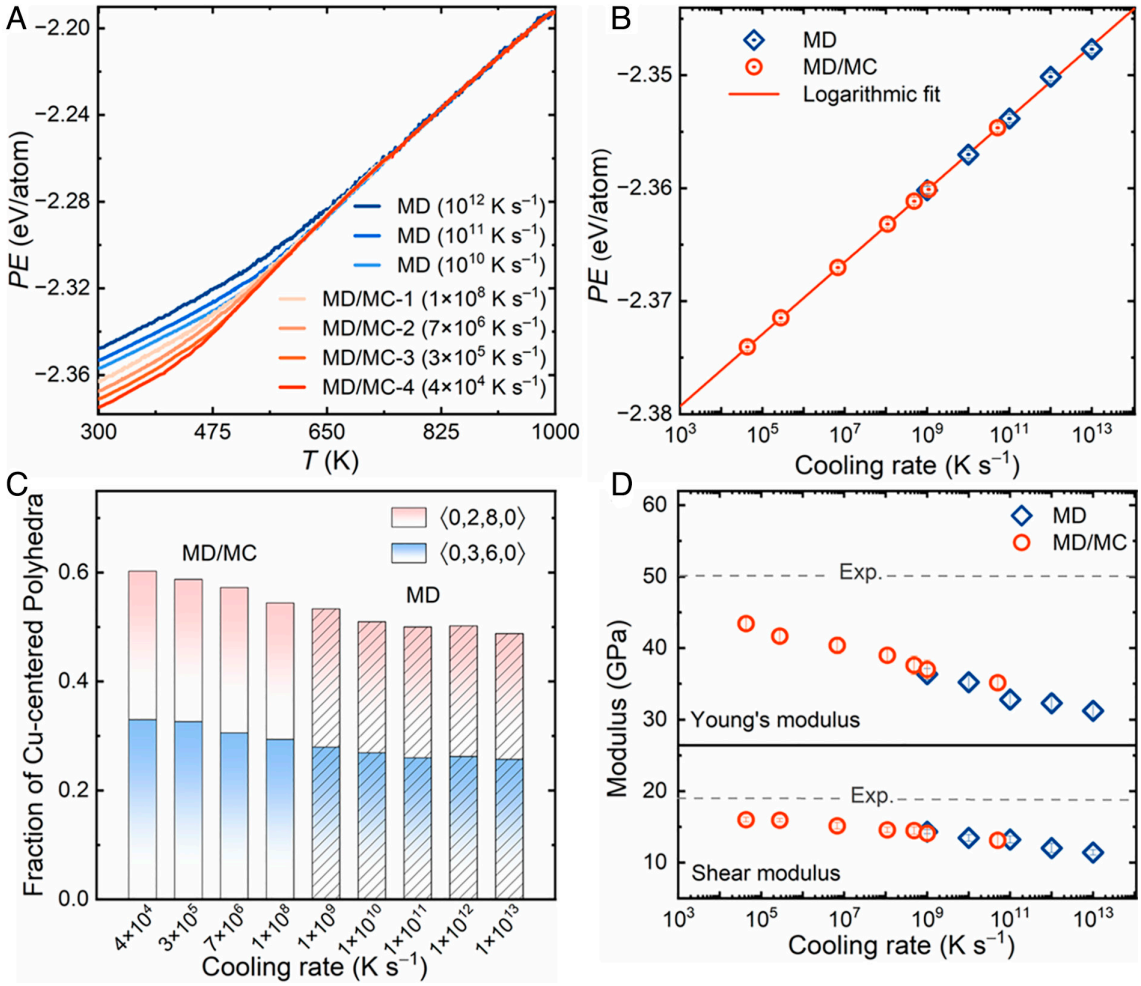

Fig. 1. $Mg_{65}Cu_{25}Y_{10}$ MG models prepared using various effective cooling rates. (*A*) Variation in per-atom potential energy (*PE*) with temperature (*T*) for different quenching rates. (*B*) Per-atom potential energy estimated at 300 K versus effective cooling rate; the solid line represents a logarithmic fit of the MD simulation data. (*C*) Fraction of Cu-centered ⟨0, 3, 6, 0⟩ and ⟨0, 2, 8, 0⟩ Frank-Kasper polyhedra. (*D*) Variation of shear modulus and Young's modulus across different effective cooling rates, with horizontal dashed lines indicating experimental values (37).

analysis of the local atomic environment out to the second nearest-neighbor shell (38) confirmed that all samples remain completely amorphous, with no evidence of crystallization (see *SI Appendix*, Fig. S1*A* for the pair distribution function). Additionally, Voronoi tessellation analysis was employed to investigate the short-range order (SRO) motifs within the samples. Fig. 1*C* presents the fractions of two characteristic Cu-centered Frank-Kasper polyhedra—tricapped trigonal prisms (Voronoi index $\langle 0, 3, 6, 0\rangle$) and bicapped square antiprisms (Voronoi index $\langle 0, 2, 8, 0\rangle$) (39). The population fractions of these polyhedral motifs are gradually reduced as the cooling rate increases, indicating subtle changes in the SRO. Moreover, the elastic constants of $Mg_{65}Cu_{25}Y_{10}$ MG samples were calculated and are shown in Fig. 1*D*. The results highlight a pronounced influence of the quenching rate on both the shear modulus (G) and Young's modulus (E). The elastic moduli obtained from regular MD simulations (cooling rates over 10^{10} K s^{-1}) differ significantly from experimental values (indicated by the dashed lines in Fig. 1*D*). However, the values obtained using the slowest cooling rate (4×10^4 K s^{-1}) from the hybrid MD/MC scheme align more closely with experimental observations (37, 40, 41).

Beyond G and E, Poisson's ratio (ν) is another critical elastic property that has been widely recognized as an indicator of the deformation behavior of MGs. Conventional MD simulations have struggled to reproduce this property due to the significant timescale gap mentioned earlier (39, 41). Specifically, the Poisson's ratio of $Mg_{65}Cu_{25}Y_{10}$ MGs prepared via traditional MD simulations is approximately 0.40, substantially higher than experimental values, which range from 0.302 to 0.329 (42, 43). However, as depicted in Fig. 2*A*, utilizing the hybrid MD/MC approach, we have successfully extended the range of Poisson's ratio for $Mg_{65}Cu_{25}Y_{10}$ MG model-samples, going down from 0.435 to 0.335, the latter aligning closely with the experimentally reported values. This opens the opportunity for a direct comparison of the simulated MG with experimental ones. Furthermore, simulated uniaxial tension was applied to the $Mg_{65}Cu_{25}Y_{10}$ MG model-samples, to observe their deformation modes including shear banding and eventual failure (see details in *Methods*). The stress–strain curves in Fig. 2*B* reveal a transition from a gradual decrease to an abrupt drop of the tensile stress after yielding, as the effective cooling rate decreases. This transition is further visualized by the snapshots showing the distribution of microscopic von Mises strain at a tensile strain of 12%, as presented in Fig. 2*C*. Two markedly different deformation modes are observed: For cooling rates exceeding 10^9 K s^{-1}, the $Mg_{65}Cu_{25}Y_{10}$ MGs exhibit delocalized plastic deformation without the formation of localized SBs. Conversely, at cooling rates below 10^9 K s^{-1}, a single SB predominates as the primary deformation mode, with the localization becoming more pronounced as the cooling rate decreases. These findings indicate that lower cooling rates significantly alter the shear banding behavior in MGs, providing a suitable platform for studying MGs that more closely replicate those produced under laboratory conditions.

Local Properties Inside the SBs. To further elucidate the microscopic properties of SBs in $Mg_{65}Cu_{25}Y_{10}$ MGs, we analyzed two representative model-samples: one with an effective cooling rate of 10^9 K s^{-1} (denoted as hyperquenched) and another with an effective cooling rate of 4×10^4 K s^{-1} (denoted as slowly cooled). Fig. 3*A* illustrates the characteristic SBs, which propagate through the MG samples at a critical strain of 12.05% for the hyperquenched sample and 7.85% for the slowly cooled sample (see *SI Appendix*, Fig. S1 *B–D*, for the definition of critical strain).

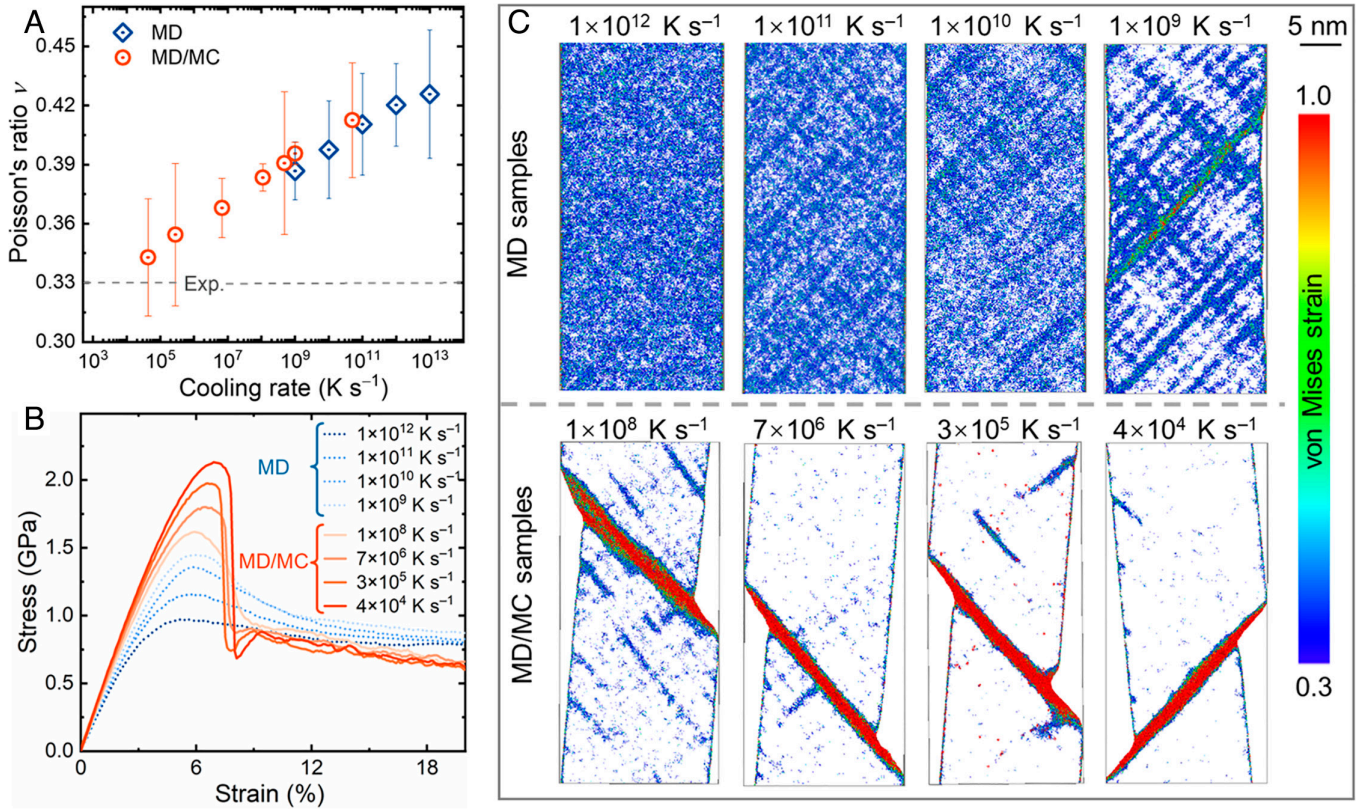

Fig. 2. Different deformation behaviors in $Mg_{65}Cu_{25}Y_{10}$ MG models. (*A*) Poisson's ratio (ν) across various effective cooling rates, with the horizontal dashed line indicating experimental values from ref. 37. (*B*) Stress–strain curves under uniaxial tension. (*C*) Snapshots of MG samples at a tensile strain of 12%, with color coding representing atomic von Mises strain (range: 0.3 to 1.0). Atoms with values less than 0.3 are excluded to highlight SBs; the *Top* panel displays MD samples, while the *Bottom* panel shows MD/MC samples.

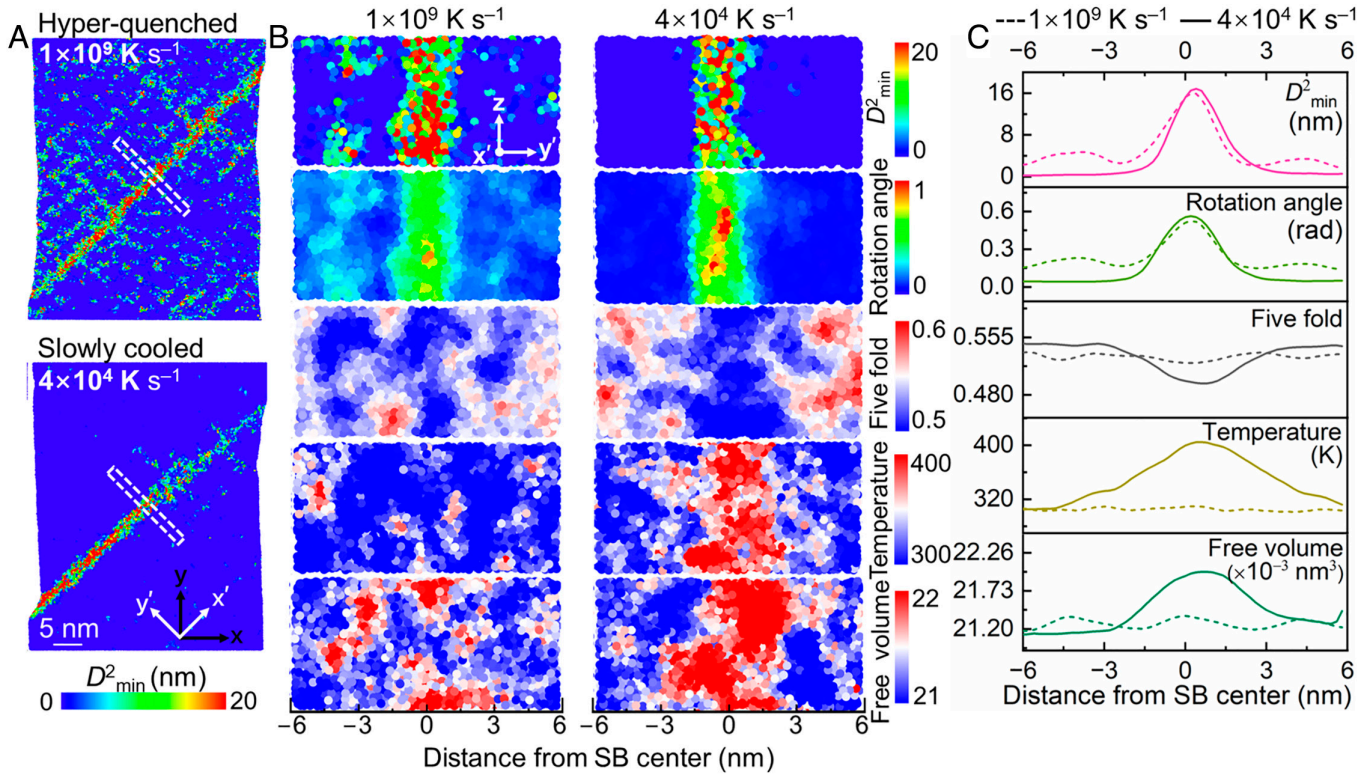

Fig. 3. Microscopic properties of SBs in hyperquenched and slowly cooled $Mg_{65}Cu_{25}Y_{10}$ MG models. (*A*) Schematic diagrams of SBs within the hyperquenched sample and slowly cooled sample, prepared at cooling rates of 1×10^9 and 4×10^4 K s^{-1}, respectively. The dashed boxes indicate the midpoint regions of the SBs at critical strains of 12.05% (hyperquenched sample) and 7.85% (slowly cooled sample). (*B*) Spatial distribution maps of microscopic D^2_{min}, rotation angle, fivefold symmetry, temperature, and free volume for both the hyperquenched sample and slowly cooled sample in the regions indicated by the dashed boxes in *A*. (*C*) Line profiles of microscopic D^2_{min}, rotation angle, local fivefold symmetry, temperature, and free volume, perpendicular to the corresponding SBs (in the y′ direction) for both the hyperquenched sample (dashed curve) and slowly cooled sample (solid curve).

We next focused on regions located at the midpoint in the thickness of each SB (indicated by dashed boxes in Fig. 3*A*), aiming to investigate the local properties of the SBs. These regions, with dimensions of $1.0 \times 12.0 \times 5.8$ nm^3 ($x' \times y' \times z$), were selected for detailed analysis of microscopic nonaffine squared displacement D^2_{min} (44), rotation angle, fivefold symmetry, temperature, and free volume (von Mises strain and volume strain, see *SI Appendix*, Fig. S2 for additional data). The spatial-distribution maps and line profiles of these properties are shown in Fig. 3 *B* and *C*, respectively. Compared with the surroundings, the central regions of both SBs exhibit an increase in D^2_{min} and rotation angle, coupled with a decrease in fivefold symmetry, consistent with previous findings that report similar trends accompanied by significant von Mises strain and volume strain (24, 45, 46).

However, the SB property rise/dip is more pronounced in the slowly cooled sample (e.g., the solid curves in Fig. 3*C*) compared to those in the hyperquenched sample. Additionally, while the temperature in the center of the SB in the hyperquenched sample remains relatively constant around 300 K, the temperature at the center of the SB in the slowly cooled sample shows a substantial increase of approximately 100 K. For comparison, the corresponding microscopic properties of SBs in the slowly cooled sample at 12.05% strain are also included in *SI Appendix*, Fig. S3.

Microscopic Mechanism of SB Propagation. Fig. 4 present microscopic maps and line profiles of initial fivefold symmetry (F_{5_ini}), D^2_{min}, rotation angle, and atomic displacement fields in two representative model samples: the hyperquenched (10^9 K s^{-1}) and slowly cooled (4×10^4 K s^{-1}) configurations, with the SB propagating halfway through the sample, approximately 20 nm from the notch. The SB front is defined as the region where atoms, exhibiting D^2_{min} greater than 20, lose their nearest neighbors for the first time in the direction of SB propagation. F_{5_ini}, derived from predeformation atomic configurations, describes the local structure of MGs. In atomistic simulations, D^2_{min} is a widely used metric to identify STZs, while rotation angles and displacement field are used to describe the collective atomic motion, particularly the vortex-like field at the SB front. As such, the results of Fig. 4 aim to sufficiently demonstrate how the local structural state governs SB propagation behavior.

In the hyperquenched MG sample (*Left* panel of Fig. 4), the region ahead of the propagating SB exhibits pronounced nanoscale heterogeneity (quantified by F_{5_ini}, Fig. 4 *A* and *B*), with strong fluctuations between structural softness and hardness, as indicated by the line profiles (each data point is obtained by averaging atomic values within a 0.5 nm bin along the SB direction). These structurally softer regions are preferentially activated into STZs, as shown by the high D^2_{min} values (Fig. 4 *C* and *D*) and are associated with quadrupolar displacement fields, forming a highly discontinuous pattern with several isolated regions. This is consistent with previous MD simulation studies (17). The displacement field around each STZ exhibits an Eshelby-like quadrupolar distribution, decaying rapidly from the STZ center to the surrounding matrix. The intervening structurally harder regions give rise to vortex-like displacements (Fig. 4 *E*–*G*). Each vortex core aligns with a peak in the rotation angle and a corresponding valley in displacement (marked by the letters "V, O, R, T, E, X" in Fig. 4*F* and the shaded regions in Fig. 4*G*), demonstrating an anticorrelated relationship between rotation angle and displacement. This results in an intermittent SB propagation mode, where discrete STZs sequentially activate and coalesce.

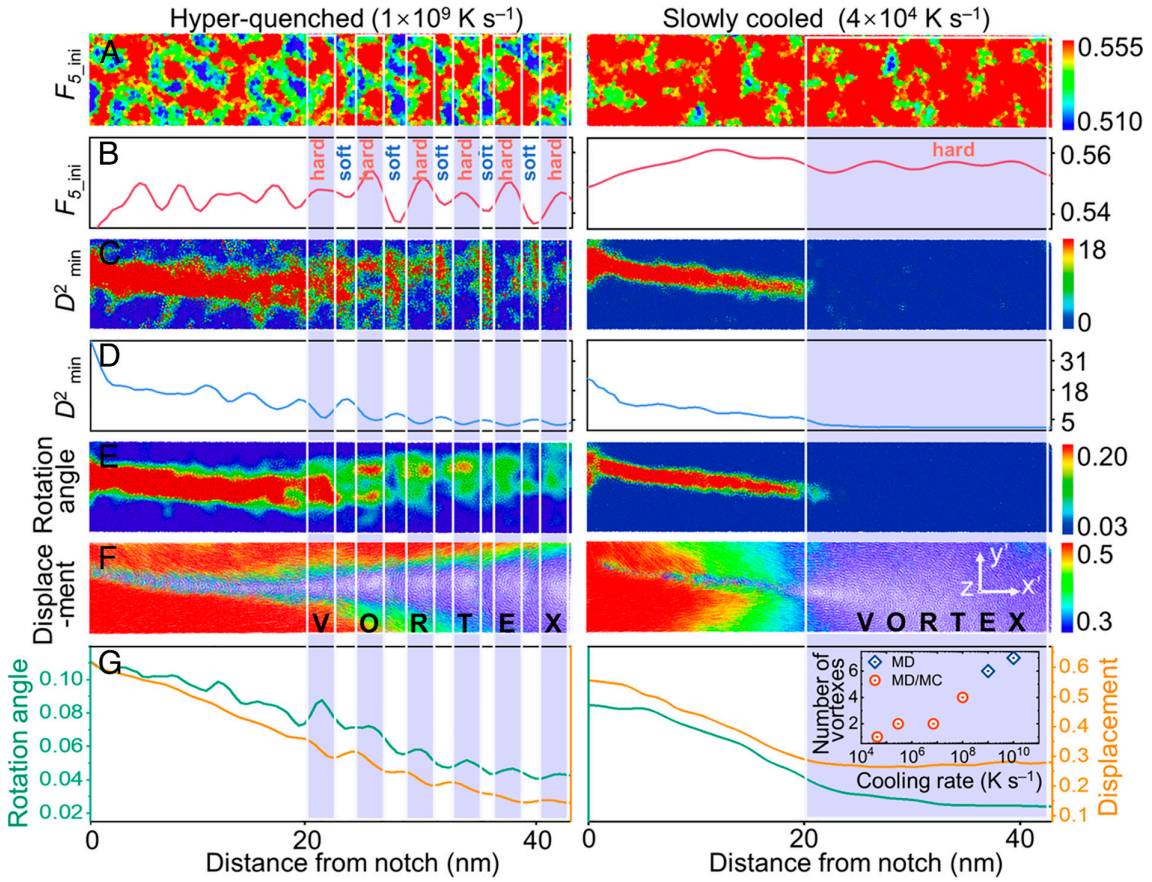

Fig. 4. Atomic-level mechanisms at the SB front as it propagates halfway through the sample. The *Left* panels correspond to hyperquenched and the *Right* panels correspond to slowly cooled samples. (*A* and *B*) Local initial fivefold symmetry (F_{5_ini}) maps and line profile; (*C* and *D*) nonaffine displacement (D^2_{min}, nm) map and line profile; (*E*–*G*) rotational angle, atomic displacement field map and their line profiles. Each line profile is averaged over 0.5 nm bins along the SB direction. The shade white solid boxes in (*A*–*G*) indicate the regions with vortex fields (also marked by the letter "V, O, R, T, E, X" in *F*). The *Inset* in the *Right* panel of (*G*) depicts the number of vortices formed at the SB front in $Mg_{65}Cu_{25}Y_{10}$ MG model-samples prepared at various cooling rates.

In contrast, the slowly cooled MG sample (*Right* panel of Fig. 4) demonstrates a contrasting local structure and its corresponding SB propagation mechanism. It shows structural homogeneity ahead of the SB front, with suppressed fluctuations in F_{5_ini} (Fig. 4 *A* and *B*). With the absence of soft regions ahead of the SB front, STZ activation is strongly inhibited (Fig. 4 *C* and *D*), and the SB propagates primarily through shear softening. The displacement field in the front of the SB follows a perfect vortex-like pattern, with minimal fluctuations in rotation angle and displacement (Fig. 4 *E*–*G*). This indicates a more homogeneous microscopic mechanism ahead of the SB front in the slowly cooled MG, characterized by smaller variations but larger-scale cooperative motion (marked with a white solid rectangle), compared to the hyperquenched MG.

Thus, the comparison between hyperquenched and slowly cooled MGs in Fig. 4 clearly demonstrates how their local structures (nanoscale heterogeneity of structural softness and hardness versus structural homogeneity with negligible soft regions) govern the distinctive SB propagation behavior: multiple discontinuous Eshelby-like features and vortex displacements versus continuous propagation with larger-scale cooperative motion. This aligns with the long-standing notion in materials science that local structure provides the multidimensional information necessary to describe the complex mechanical response of MGs, beyond what a single scalar quantity, such as total energy, can convey. While local structure and total energy are closely linked in MGs, they are not interchangeable, especially in determining plastic deformation (47, 48). Other local features, such as local potential energy, can also significantly influence STZ activation and SB propagation mechanisms (*SI Appendix*, Fig. S4).

In *SI Appendix*, Fig. S5, the D^2_{min} and displacement of SBs propagating up to one-third (14 nm) of the way through the samples are plotted, further confirming that the distinct propagation mechanisms of SBs persist throughout the entire process, with the propagation pattern changing with sample cooling rate. Displacement plots at different cooling rates show a reduction in the number of vortex fields ahead of the SB front with decreasing cooling rates, transitioning from multiple small vortices to a single large vortex field, as depicted in the *Inset* of Fig. 4*G*. This highlights a major transition, in terms of the SB propagation mechanism, from the hyperquenched to slowly cooled MG models.

Fig. 5 schematically illustrates the distinct mechanisms underlying the propagation patterns of SBs in hyperquenched and slowly cooled MG samples. Upon application of a load, the region near the notch initially generates a strong stress field. In the hyperquenched sample (Fig. 5*A*), nanoscale fluctuations in structural hardness and softness enable the activation of STZs within soft regions, while the vortex field (with stress concentration, see *SI Appendix*, Fig. S4) is induced by two adjacent STZs, characterized by a quadrupolar Eshelby-like distribution. As the load increases, multiple discontinuous STZs, separated by vortices, are sequentially activated, propagating and eventually coalescing to form a SB. This results in an intermittent SB propagation pattern. In contrast, in the slowly cooled sample (Fig. 5*B*), which exhibits structural homogeneity of hardness, the stress field generated by the vortex-like motion is insufficient to induce or activate

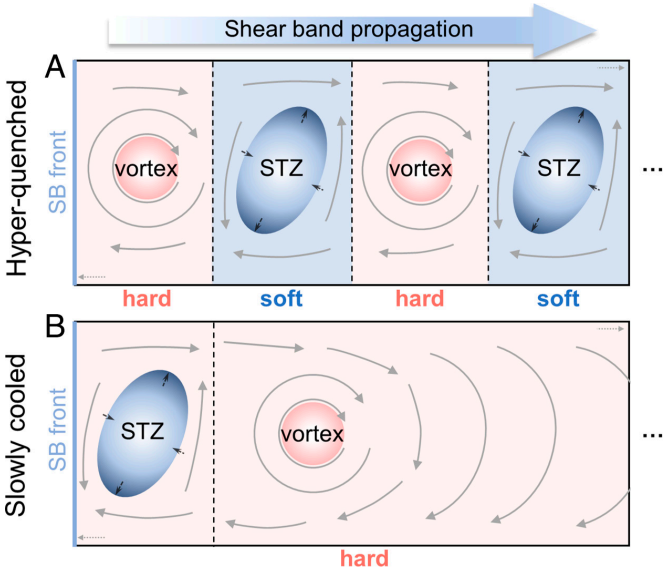

Fig. 5. Schematic diagrams of the mechanisms of SB propagation. (*A*) Hyperquenched and (*B*) slowly cooled MG models. The blue bolded line represents the front of SB propagation. The structurally soft (blue) and hard (pink) regions are directly responsible for STZs (ellipsoids) and vortex centers (circles), respectively. Gray arrows indicate the directions of local atomic motions.

neighboring regions to form multiple STZs. Instead, SB propagation in slowly cooled samples primarily relies on shear softening at the SB tip, activating STZs in the immediate vicinity of the SB front, followed by the formation of a large vortex field due to the homogeneous structure dominated by solid-like regions. Consequently, SB propagation occurs in a continuous manner, characteristic of brittle fracture in materials.

It is important to note that the SB propagation mechanism can be influenced by the significant difference in energy release upon SB formation between hyperquenched and slowly cooled samples. As shown in Fig. 2*B*, the energy release is reflected by the transition from maximum stress to flow stress. The flow stress is only weakly dependent on the cooling rate because, once the flow begins, the system reaches a pseudoequilibrium steady state, effectively eliminating the effects of thermal history (49–51). To minimize the influence of energy release, such as temperature rise within the shear band, additional MD simulations were conducted, where the shear band configurations were unloaded halfway through the sample (e.g., Fig. 4) and relaxed at 300 K (*SI Appendix*, Fig. S6 *A–D*). Upon reloading, both MGs continued to exhibit their characteristic SB propagation modes: sequential activation and coalescence of multiple STZs in the hyperquenched sample versus continuous SB propagation in the slowly cooled sample (*SI Appendix*, Fig. S6 *E* and *F*). This analysis confirms that the differences in SB propagation are primarily attributed to the structural states induced by the cooling rates, rather than being solely due to transient effects caused by energy release during the stress drop.

Kinetics of SB Propagation. Understanding the dynamics of initial SB propagation is essential for elucidating the mechanisms underlying shear banding in MGs. By examining the morphological changes of SBs segment-by-segment during propagation, we identified significant differences between the SB propagation behaviors in hyperquenched and slowly cooled samples.

For the hyperquenched sample, the morphology of the SBs reveals a "stop-and-go" propagation pattern, taking approximately 175 ps to advance 10 nm (Fig. 6*A*). This behavior results from the activation of multiple, discontinuous STZs along the SB propagation path, as described earlier. Under applied stress, the SB propagates by gradually linking these STZ regions. This mode of propagation leads to a longer "incubation period" during SB propagation, i.e., it takes more time to connect to the next STZ region.

In contrast, the slowly cooled sample exhibits significantly faster SB propagation, with 10 nm covered in only 35 ps (Fig. 6*B*). In this sample, the SB advances in a continuous and stable manner, resulting in a steady increase in propagation velocity, unlike the intermittent propagation observed in the hyperquenched sample. The *Inset* in Fig. 6*B* quantifies this difference by showing the displacement change of the SB ($\Delta d = d_i - d_0$) (approximately 10 nm) over time for both samples, where d_i is the position of the SB at time i, and d_0 is the initial position. This clearly illustrates the intermittent nature of SB propagation in the hyperquenched sample compared to the continuous progression in the slowly cooled sample.

Fig. 6*C* presents the SB propagation velocity as a function of propagation distance. Here, the SB is composed of atoms with shear strain larger than a threshold value $\gamma_c = 0.1$. (We have found that for $\gamma_c \geq 0.10$, the morphology (and hence the kinetics) of the SB propagation is more or less converged, see *SI Appendix*, Fig. S7 for the influence of γ_c). Initially, the SB propagation velocity is relatively low in both samples but increases as the SB advances. When the SB length reaches about one-fourth (10 nm) of the sample width, significant differences in propagation velocity emerge between the two samples: the SBs propagate faster in the model-sample formed at lower cooling rate. Notably, the SB propagation velocities in our simulated MGs are somehow in between those reported in previous simulations (52, 53) and experimental studies (54–56). This discrepancy in simulations could result from differences in stress states and measurement standards. For example, in ref. 53, the SB velocity measured using the perturbative static loading method for a Lennard-Jones sample with a tensile strain of 3.4% is approximately 1,000 m s^{-1}, faster than those in Fig. 6*C*. Differences in sample type and load/straining conditions can lead to different velocities. Additionally, the SB propagation velocity in the slowly cooled sample without a notch is approximately five times higher than in the notched sample (*SI Appendix*, Fig. S8). The higher stress accumulated/released for SB activation/propagation results in a larger SB propagation speed as compared to the case without a notch.

Fig. 6*D* illustrates the relationship between SB propagation distance and time. For samples cooled at lower rates, SB propagation is continuous, whereas in samples with higher cooling rates, propagation is intermittent, aligning with the differences in SB propagation mechanism across various cooling rates. The intermittent propagation of the SB can be divided into "incubation time," representing pauses in propagation, and "forward time," representing a period of continuous march-forward. Fig. 6*E* shows the ratio of forward time to incubation time as a function of cooling rate. It is evident that as the cooling rate decreases, the proportion of incubation time diminishes while the proportion of forward time increases, indicating a shorter overall time required for SB propagation.

Conclusion

This study provides insights into the microscopic mechanisms underlying SB-propagation in $Mg_{65}Cu_{25}Y_{10}$ MG model samples across the transition from "hyperquenched" states to "slowly cooled" states. By employing a combination of MD and hybrid MD/MC simulations, we explored the effects of sample cooling rate on SB behavior, uncovering distinctly different propagation mechanisms in hyperquenched and slowly cooled MGs. We find that, in hyperquenched MGs, SB propagation is "stop-and-go",

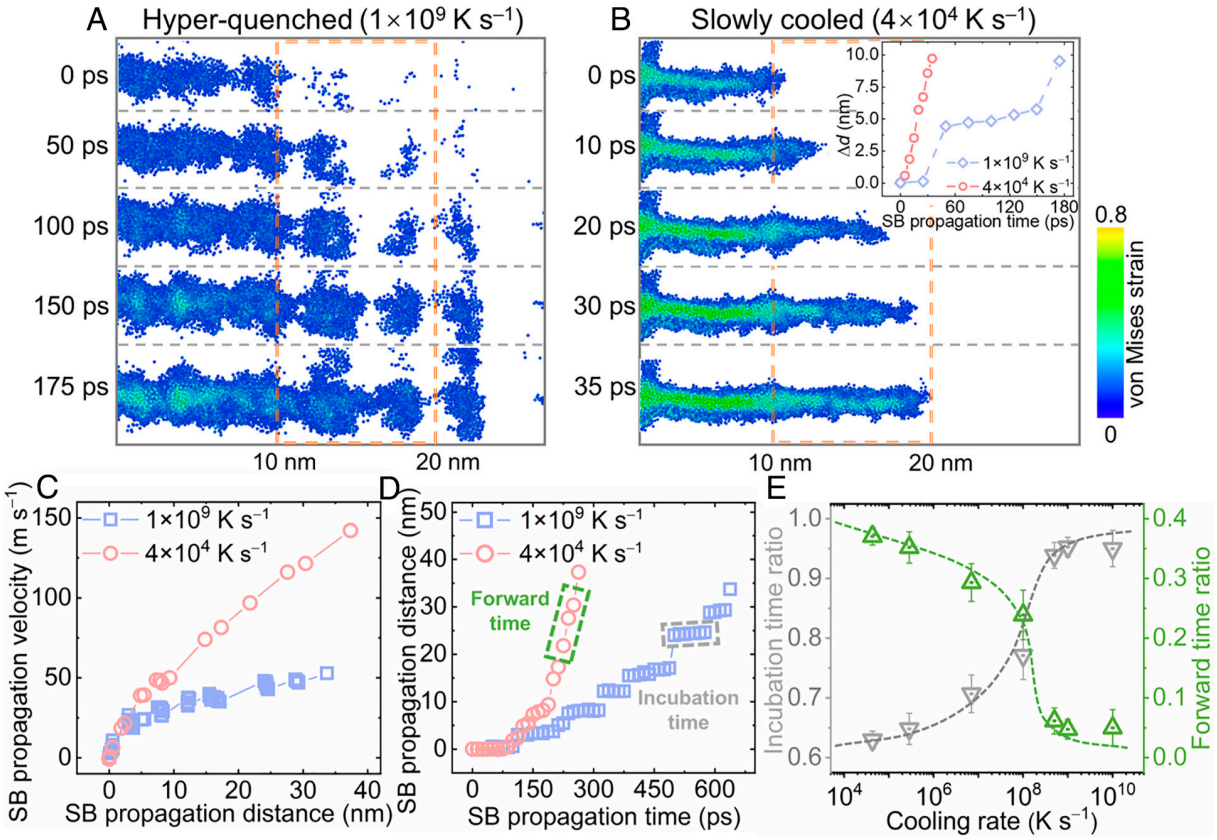

Fig. 6. Kinetics of SB propagation. (*A* and *B*) Schematic representation of SB morphology as it progresses from one-fourth (10 nm) to halfway (20 nm) through the sample. (*A*) Depicts the hyperquenched sample, (*B*) shows the slowly cooled sample. Atoms with von Mises strain less than 0.1 are removed for clarity. The dashed boxes highlight SB progression from 10 to 20 nm within the sample. The *Inset* in (*B*) shows the displacement variation (Δd) for the two samples over time. (*C*) SB propagation velocity as a function of propagation distance. (*D*) SB propagation distance as a function of propagation time. See *SI Appendix*, Fig. S9 for results from other samples. (*E*) Percentages of "forward time" and "incubation time" as functions of cooling rate, with error bars representing SD. Dashed lines are included as visual guides.

arising from the sequential activation and coalescence of multiple STZs interspersed with vortex-like fields ahead of the SB front. In contrast, slowly cooled MGs exhibit continuous, rapid SB propagation, mediated by localized shear-softening effects and dominated by large vortex fields, reflecting a more homogeneous response from the MG structure. It would be interesting to see in the future whether the SB mechanisms unraveled in this work are generic to other families of MGs.

The methodology developed and applied in this work—combining advanced simulation techniques with comprehensive microscopic analysis—offers a robust approach for investigating complex deformation mechanisms in amorphous materials. This research not only elucidates the atomic-scale processes that govern SB initiation dynamics in MGs, but also opens avenues for the controlled manipulation of mechanical properties. In particular, the role of MG structural states and its impact on the mechanical properties of these materials is highlighted. Future studies can build upon these findings to explore the broader implications of these mechanisms in different alloy systems and under different loading conditions, thereby contributing to the design and optimization of next-generation MGs with enhanced performance and reliability to target specific mechanical properties and applications.

Methods

MD-Simulated $Mg_{65}Cu_{25}Y_{10}$ MGs. The MD simulations in this study employed the embedded-atom-method potentials developed in ref. 39, which are well suited for simulating amorphous Mg–Cu–Y alloys, even at relatively low cooling rates. We generated $Mg_{65}Cu_{25}Y_{10}$ MG samples using both a conventional MD approach and a hybrid MD/MC method (57). For the pure MD simulations, a standard melt-quench procedure was utilized to obtain glass samples of various system sizes. Periodic boundary conditions were applied in all three dimensions. Initially, a cubic box containing 10,000 atoms was heated to 1,500 K for 2 ns. The equilibrated liquid sample was then cooled from 1,500 K to 300 K at various cooling rates, ranging from 10^9 to 10^{13} K s^{-1} using isothermal–isobaric ensemble under zero pressure (58–60). Following quenching, the glass sample was further relaxed at 300 K for 2 ns, which is sufficient to ensure convergence of the glass properties.

$Mg_{65}Cu_{25}Y_{10}$ MGs Prepared by Hybrid MD/MC Approach. The hybrid MD/MC approach utilized a novel algorithm described in ref. 57, allowing for local atomic swaps during the MC steps, while relaxations were accounted for by the MD integration steps. This hybrid scheme interrupts standard MD dynamics to achieve more efficient structural relaxation. Simulations were conducted in the variable-cell semigrand canonical ensemble with a variance parameter κ set to 1,000 effectively integrated into the LAMMPS simulation package (61). The MC temperature, which determines the Metropolis acceptance criterion, was set equal to the MD temperature. For samples produced using the hybrid MD/MC scheme, the resulting glass samples were further relaxed using the pure MD scheme at 300 K for 2 ns before assessing their properties.

Mechanical Deformation Simulation. To investigate SB formation, uniaxial tension simulations were performed. A glass sample containing 10,000 atoms was replicated 7 times along the *x*-axis and 14 times along the *y*-axis, resulting in a larger sample with dimensions of 41.6 × 83.1 × 5.94 nm^3 (*x*-*y*-*z*) containing 980,000 atoms. Previous studies have demonstrated that replicating smaller samples does not affect the deformation behavior of MG models and is a cost-effective approach (36). The entire process was conducted under a zero-pressure isothermal-isobaric ensemble with periodic boundary conditions. The periodic boundary condition in the x-direction was subsequently

removed, and the sample was relaxed for 1 ns to create a free surface. The samples were then subjected to uniaxial tension along the y-axis at a strain rate of 2×10^7 s^{-1} at 300 K. A timestep of 2 fs was used in the simulations, with a Nosé–Hoover thermostat and a barostat (58–60) to control the temperature and pressure, respectively.

Local Structural Analysis. To characterize the local structure of the alloy, Voronoi tessellation was employed. The local fivefold symmetry around the central atom i is defined as $F_5 = n_5/(n_3 + n_4 + n_5 + n_6)$, where n_j (j = 3, 4, 5, 6) is the number of j edges in a Voronoi polyhedron. Atomic-scale properties such as von Mises strain, volumetric strain, nonaffine squared displacement (D^2_{min}), rotation angle, and displacement vectors were calculated and visualized using OVITO software (62). The cutoff radius, of about 0.68 nm, was selected to encompass two nearest-neighbor coordination shells.

Data, Materials, and Software Availability. Data generated or analyzed during this study are included in the article and/or *SI Appendix*.

ACKNOWLEDGMENTS. This work was funded by the National Natural Science Foundation of China (No. 52231001, 12004294), State Key Laboratory for Advanced Metals and Materials (2024-Z15), National Youth Talents Program and the HPC platform of Xi'an Jiaotong University. J.D. and E.M. are indebted to Xi'an Jiaotong University for hosting their work at the Center for Alloy Innovation and Design. Z.Z. acknowledges the National Natural Science Foundation of China (No. 12474185), Z.S. acknowledges the National Natural Science Foundation of China (No. 12372116).

Author affiliations: [a]Center for Alloy Innovation and Design, State Key Laboratory for Mechanical Behavior of Materials, Xi'an Jiaotong University, Xi'an 710049, China; [b]Department of Physics, Chengdu University of Technology, Chengdu 610059, China; [c]State Key Laboratory for Strength and Vibration of Mechanical Structures, School of Aerospace Engineering, Xi'an Jiaotong University, Xi'an 710049, China; [d]Department of Materials Science and Metallurgy, University of Cambridge, Cambridge CB3 0FS, United Kingdom; and [e]World Premier International Advanced Institute for Materials Research, Tohoku University, Sendai 980-8577, Japan

1. C. M. Gourlay, A. K. Dahle, Dilatant shear bands in solidifying metals. *Nature* **445**, 70–73 (2007).
2. A. Wisitsorasak, P. G. Wolynes, Dynamical theory of shear bands in structural glasses. *Proc. Natl. Acad. Sci. U.S.A.* **114**, 1287–1292 (2017).
3. G. Ma, W. Zhou, X.-l. Chang, T. T. Ng, L.-f. Yang, Formation of shear bands in crushable and irregularly shaped granular materials and the associated microstructural evolution. *Powder Technol.* **301**, 118–130 (2016).
4. A. Fall, F. Bertrand, G. Ovarlez, D. Bonn, Yield stress and shear banding in granular suspensions. *Phys. Rev. Lett.* **103**, 178301 (2009).
5. A. L. Greer, Y. Q. Cheng, E. Ma, Shear bands in metallic glasses. *Mater. Sci. Eng. R Rep.* **74**, 71–132 (2013).
6. A. S. Argon, Plastic deformation in metallic glasses. *Acta Metall.* **27**, 47–58 (1979).
7. C. A. Schuh, A. C. Lund, Atomistic basis for the plastic yield criterion of metallic glass. *Nat. Mater.* **2**, 449–452 (2003).
8. V. Hieronymus-Schmidt, H. Rösner, G. Wilde, A. Zaccone, Shear banding in metallic glasses described by alignments of Eshelby quadrupoles. *Phys. Rev. B* **95**, 134111 (2017).
9. O. Glushko, R. Pippan, D. Şopu, C. Mitterer, J. Eckert, How to catch a shear band and explain plasticity of metallic glasses with continuum mechanics. *Nat. Commun.* **15**, 5601 (2024).
10. S. Takeuchi, K. Edagawa, Atomistic simulation and modeling of localized shear deformation in metallic glasses. *Prog. Mater. Sci.* **56**, 785–816 (2011).
11. A. Vinogradov, M. Seleznev, I. S. Yasnikov, Dislocation characteristics of shear bands in metallic glasses. *Scr. Mater.* **130**, 138–142 (2017).
12. R. Dasgupta, H. G. E. Hentschel, I. Procaccia, Microscopic mechanism of shear bands in amorphous solids. *Phys. Rev. Lett.* **109**, 255502 (2012).
13. C. E. Maloney, A. Lemaître, Amorphous systems in athermal, quasistatic shear. *Phys. Rev. E* **74**, 016118 (2006).
14. F. Shimizu, S. Ogata, J. Li, Theory of shear banding in metallic glasses and molecular dynamics calculations. *Mater. Trans.* **48**, 2923–2927 (2007).
15. D. Srolovitz, V. Vitek, T. Egami, An atomistic study of deformation of amorphous metals. *Acta Metall.* **31**, 335–352 (1983).
16. Y. Gao, A cavity-based micromechanical model for the shear-band failure in metallic glasses under arbitrary stress states. *J. Appl. Mech.* **90**, 4714–4728 (2023).
17. D. Şopu, A. Stukowski, M. Stoica, S. Scudino, Atomic-level processes of shear band nucleation in metallic glasses. *Phys. Rev. Lett.* **119**, 195503 (2017).
18. H. Sheng, D. Şopu, S. Fellner, J. Eckert, C. Gammer, Mapping shear bands in metallic glasses: From atomic structure to bulk dynamics. *Phys. Rev. Lett.* **128**, 245501 (2022).
19. D. Şopu, S. Scudino, X. L. Bian, C. Gammer, J. Eckert, Atomic-scale origin of shear band multiplication in heterogeneous metallic glasses. *Scr. Mater.* **178**, 57–61 (2020).
20. D. Şopu, STZ-vortex model: The key to understand STZ percolation and shear banding in metallic glasses. *J. Alloys Compd.* **960**, 170585 (2023).
21. S. Kang *et al.*, Direct observation of quadrupolar strain fields forming a shear band in metallic glasses. *Adv. Mater.* **35**, 2212086 (2023).
22. M. Hassani, A. E. Lagogianni, F. Varnik, Probing the degree of heterogeneity within a shear band of a model glass. *Phys. Rev. Lett.* **123**, 195502 (2019).
23. H. Zhou, L. Shen, B. Sun, W. Wang, Research progress on the shear band of metallic glasses. *J. Alloys Compd.* **955**, 170164 (2023).
24. A. J. Cao, Y. Q. Cheng, E. Ma, Structural processes that initiate shear localization in metallic glass. *Acta Mater.* **57**, 5146–5155 (2009).
25. D. Şopu *et al.*, From elastic excitations to macroscopic plasticity in metallic glasses. *Appl. Mater. Today* **22**, 100958 (2021).
26. J. Ding, Y. Q. Cheng, E. Ma, On the origin of elastic limit of bulk metallic glasses. *Appl. Phys. Lett.***104,** 011912 (2014).
27. E. R. Homer, Examining the initial stages of shear localization in amorphous metals. *Acta Mater.* **63**, 44–53 (2014).
28. F. Shimizu, S. Ogata, J. Li, Yield point of metallic glass. *Acta Mater.* **54**, 4293–4298 (2006).
29. K. Vollmayr, W. Kob, K. Binder, How do the properties of a glass depend on the cooling rate? A computer simulation study of a Lennard-Jones system. *J. Chem. Phys.* **105**, 4714–4728 (1996).
30. Y. Zhang *et al.*, Cooling rates dependence of medium-range order development in Cu64.5Zr35.5 metallic glass. *Phys. Rev. B* **91**, 064105 (2015).
31. M. Fan *et al.*, Effects of cooling rate on particle rearrangement statistics: Rapidly cooled glasses are more ductile and less reversible. *Phys. Rev. E* **95**, 022611 (2017).
32. R. E. Ryltsev, B. A. Klumov, N. M. Chtchelkatchev, K. Y. Shunyaev, Cooling rate dependence of simulated Cu64.5Zr35.5 metallic glass structure. *J. Chem. Phys.* **145**, 034506 (2016).
33. L. Berthier, D. Coslovich, A. Ninarello, M. Ozawa, Equilibrium sampling of hard spheres up to the jamming density and beyond. *Phys. Rev. Lett.* **116**, 238002 (2016).
34. T. S. Grigera, G. Parisi, Fast Monte Carlo algorithm for supercooled soft spheres. *Phys. Rev. E* **63**, 045102 (2001).
35. A. D. S. Parmar, M. Ozawa, L. Berthier, Ultrastable metallic glasses in silico. *Phys. Rev. Lett.* **125**, 085505 (2020).
36. Z. Zhang, J. Ding, E. Ma, Shear transformations in metallic glasses without excessive and predefinable defects. *Proc. Natl. Acad. Sci. U.S.A.* **119**, e2213941119 (2022).
37. X. K. Xi, R. J. Wang, D. Q. Zhao, M. X. Pan, W. H. Wang, Glass-forming Mg–Cu–RE (RE=Gd, Pr, Nd, Tb, Y, and Dy) alloys with strong oxygen resistance in manufacturability. *J. Non-Cryst. Solids* **344**, 105–109 (2004).
38. E. Maras, O. Trushin, A. Stukowski, T. Ala-Nissila, H. Jónsson, Global transition path search for dislocation formation in Ge on Si(001). *Comput. Phys. Commun.* **205**, 13–21 (2016).
39. J. Ding, Y. Cheng, E. Ma, Charge-transfer-enhanced prism-type local order in amorphous Mg65Cu25Y10: Short-to-medium-range structural evolution underlying liquid fragility and heat capacity. *Acta Mater.* **61**, 3130–3140 (2013).
40. A. Castellero, B. Moser, D. I. Uhlenhaut, F. H. D. Torre, J. F. Löffler, Room-temperature creep and structural relaxation of Mg–Cu–Y metallic glasses. *Acta Mater.* **56**, 3777–3785 (2008).
41. J. Q. Wang, P. Yu, H. Y. Bai, Minor addition induced enhancement of strength of Mg-based bulk metallic glass. *J. Non-Cryst. Solids* **354**, 5440–5443 (2008).
42. W. H. Wang, Correlation between relaxations and plastic deformation, and elastic model of flow in metallic glasses and glass-forming liquids. *J. Appl. Phys.* **110**, 053521 (2011).
43. W. H. Wang, The elastic properties, elastic models and elastic perspectives of metallic glasses. *Prog. Mater. Sci.* **57**, 487–656 (2012).
44. M. L. Falk, J. S. Langer, Dynamics of viscoplastic deformation in amorphous solids. *Phys. Rev. E* **57**, 7192–7205 (1998).
45. Y. Q. Cheng, A. J. Cao, H. W. Sheng, E. Ma, Local order influences initiation of plastic flow in metallic glass: Effects of alloy composition and sample cooling history. *Acta Mater.* **56**, 5263–5275 (2008).
46. Y. Q. Cheng, A. J. Cao, E. Ma, Correlation between the elastic modulus and the intrinsic plastic behavior of metallic glasses: The roles of atomic configuration and alloy composition. *Acta Mater.* **57**, 3253–3267 (2009).
47. Y. H. Meng *et al.*, Rejuvenation by enthalpy relaxation in metallic glasses. *Acta Mater.* **241**, 118376 (2022).
48. N. Wang *et al.*, Spatial correlation of elastic heterogeneity tunes the deformation behavior of metallic glasses. *Npj Comput. Mater.* **4**, 19 (2018).
49. Y. Fan, T. Iwashita, T. Egami, Energy landscape-driven non-equilibrium evolution of inherent structure in disordered material. *Nat. Commun.* **8**, 15417 (2017).
50. J. Ding *et al.*, Universal nature of the saddle states of structural excitations in metallic glasses. *Mater. Today Phys.* **17**, 100359 (2021).
51. P. Guan, M. Chen, T. Egami, Stress-temperature scaling for steady-state flow in metallic glasses. *Phys. Rev. Lett.* **104**, 205701 (2010).
52. X. Bian *et al.*, Signature of local stress states in the deformation behavior of metallic glasses. *NPG Asia Mater.* **12**, 59 (2020).
53. J. Luo, L. Huang, Y. Shi, B. Deng, The dynamics of shear band propagation in metallic glasses. *Acta Mater.* **248**, 118787 (2023).
54. W. J. Wright, R. R. Byer, X. Gu, High-speed imaging of a bulk metallic glass during uniaxial compression. *Appl. Phys. Lett.* **102**, 241920 (2013).
55. R. Maaß, J. F. Löffler, Shear-band dynamics in metallic glasses. *Adv. Funct. Mater.* **25**, 2353–2368 (2015).
56. M. Seleznev, I. S. Yasnikov, A. Vinogradov, On the shear band velocity in metallic glasses: A high-speed imaging study. *Mater. Lett.* **225**, 105–108 (2018).
57. B. Sadigh *et al.*, Scalable parallel monte carlo algorithm for atomistic simulations of precipitation in alloys. *Phys. Rev. B* **85**, 184203 (2010).
58. S. Nosé, A unified formulation of the constant temperature molecular dynamics methods. *J. Chem. Phys.* **81**, 511–519 (1984).
59. W. G. Hoover, Canonical dynamics: Equilibrium phase-space distributions. *Phys. Rev. A* **31**, 1695–1697 (1985).
60. W. G. Hoover, Constant-pressure equations of motion. *Phys. Rev. A* **34**, 2499–2500 (1986).
61. W. Kob, H. C. Andersen, Testing mode-coupling theory for a supercooled binary Lennard-Jones mixture. II. Intermediate scattering function and dynamic susceptibility. *Phys. Rev. E* **52**, 4134–4153 (1995).
62. A. Stukowski, Visualization and analysis of atomistic simulation data with OVITO–the open visualization tool. *Model. Simul. Mater. Sci. Eng.* **18**, 015012 (2010).